Analyst

ROYAL SOCIETY OF CHEMISTRY

PAPER

View Article Online
View Journal | View Issue

Cite this: *Analyst*, 2024, **149**, 5843

Towards high-resolution water isotope analysis in ice cores using laser ablation – cavity ring-down spectroscopy†

Eirini Malegiannaki, *[a,b] Pascal Bohleber, [b,c] Daniele Zannoni, [b] Ciprian Stremtan, [d] Agnese Petteni, [b] Barbara Stenni, [b] Carlo Barbante, [b,e] Bo M. Vinther [a] and Vasileios Gkinis [a]

A new micro-destructive technique for high-resolution water isotope analysis of ice samples using a Laser Ablation (LA) system coupled with a Cavity Ring Down Spectrometer (CRDS) is presented. This method marks the first time water isotope analysis is conducted directly on the ice, bypassing the traditional steps of melting and vaporizing the ice sample, thanks to the direct transition of ice into water vapour through the laser ablation process. A nanosecond ArF laser ablation system (193 nm) with an integrated two-volume ablation chamber was successfully coupled to a CRDS analyzer, utilizing nitrogen as the carrier gas. The application goal is the use of LA-CRDS for ice core studies, so a method for preparing ice standard samples using liquid water isotope standards, widely used for ice core analysis, is introduced. The measurements were conducted in a discrete mode, by performing laser ablation raster scans of 4 mm × 4 mm areas, establishing a sampling resolution of 4 mm along an ice core's depth. The water vapour concentration reaching the CRDS analyzer as well as the quality of the water isotopic measurements of $\delta^{18}O$ and δD were influenced by laser parameters, such as laser spot size, repetition rate, laser fluence, ablation time as well as by the flow rates of the carrier gas. After optimizing the experimental conditions for water vapour formation, three ice standards samples were analyzed for calibration purposes on the VSMOW-SLAP scale and a section of an ice core sample was also tested. Critical parameters influencing the precision and accuracy of water isotopic measurements were investigated, and isotopic fractionation phenomena were identified, pointing to essential considerations for the technique's further development.

Received 2nd August 2024,
Accepted 19th October 2024

DOI: 10.1039/d4an01054j

rsc.li/analyst

1 Introduction

Polar ice core records stand as one of the most invaluable archives in paleoclimate research, providing detailed insights into environmental changes spanning from decades to hundreds of millennia.[1] The Beyond EPICA project, aiming to retrieve a 1.5 million year-old ice core from Antarctica, represents a significant step forward in this field with water isotopes serving as a pivotal parameter for past climate reconstruction and interpretation.[2] Water stable isotope ratios, which are usually reported in delta-notation ($\delta^{18}O$ and δD),[3] are fundamental to the study of past climate processes, acting as a proxy for past temperatures.[4] Ice core archives allow for the continuous experimental determination of water isotopes[5,6] which in turn enables the detailed reconstruction of climate records, improving our understanding of past atmospheric conditions and long-term climate trends. However, extracting water isotope signals from the Beyond EPICA – Oldest Ice Core presents unique analytical challenges. In the ice core's oldest and deepest sections and up to the depths where the stratigraphy is preserved, more than 10 kyr are packed into each meter of ice.[7,8] The resulting extremely thin ice layers require high-resolution sampling techniques to improve both depth and temporal resolution which will lead to high-quality signal retrieval and better interpretation of the

[a]*Physics of Ice Climate and Earth, Niels Bohr Institute, University of Copenhagen, Tagensvej 16, 2200 Copenhagen, Denmark. E-mail: eirini.malegiannaki@nbi.ku.dk*
[b]*Department of Environmental Sciences, Informatics and Statistics, Ca' Foscari University of Venice, Via Torino 155, 30172 Venice Mestre, VE, Italy*
[c]*Department of Geosciences, Alfred Wegener Institute Helmholtz Centre for Polar and Marine Research, Bremerhaven, Germany*
[d]*Teledyne Photon Machines, Bozeman, MT, USA*
[e]*Institute of Polar Sciences, National Research Council (CNR-ISP), Via Torino 155, 30172 Venice Mestre, VE, Italy*

†Electronic supplementary information (ESI) available: Humidity response of the CRDS analyzer, TEDRIST ice core cutting scheme, and LA-CRDS measurement images from the TEDRIST ice core section. See DOI: https://doi.org/10.1039/d4an01054j

climate data. The development of cutting-edge, high-resolution sampling techniques is crucial not only for extracting continuous high-resolution water isotope signals but also for investigating processes that contribute to signal attenuation or even loss in deep ice, such as the diffusion of water molecules, critical for signal restoration,[9] and the formation of water veins.[10,11]

Cavity Ring Down Spectroscopy (CRDS)[12,13] has been widely used for water stable isotope analysis on ice cores with comparable precision to the traditional IRMS analyzer.[14,15] A CRDS water isotope analyzer utilizes a high finesse optical cavity to extend the effective path length of a laser beam, enabling the ultra-sensitive detection of gas-phase molecules and producing signal for multiple water stable isotopes simultaneously ($\delta^{18}O$, δD) based on their unique near-infrared absorption characteristics. The implementation of Continuous Flow Analysis (CFA) for ice core samples[16] enabled continuous melting of the ice, which after efficient vaporization of the liquid sample and subsequent water isotope analysis by CRDS, has resulted in high-precision water isotope signals along with a depth resolution of less than 1 cm.[17–19] However, even with streamlined sample preparation in current CFA-CRDS protocols, the melting procedure can artificially alter the signal, the depth control remains challenging, and the resulting depth and temporal resolution is insufficient for resolving thin layers in the deep ice cores. This underscores the need for the development of high-resolution, minimally invasive sampling techniques.

Laser Ablation (LA) is used as a sampling method[20] that allows a minute amount of sample to turn into vapour, plasma, and particles, without any specific requirements of sample size or preparation. For analytical purposes, the ablated material is collected in an ablation chamber and transported *via* a carrier gas to an analyzer, commonly an ICP-MS (Inductively Coupled Plasma – Mass Spectrometer).[21] LA-ICP-MS exploits the particulate phase of the ablated material, introduced directly to the analyzer, for chemical analysis, leaving the ablation chamber which is flushed with a carrier gas. LA analytical power lies also in the direct analysis of the vapour produced by measuring the atomic/ionic emissions of the created plasma (LIBS).

LA has been already used both for LIBS hydrogen isotope analysis of frozen water deuteriated samples[22,23] and for ice sampling obtaining high-resolution multi-elemental analysis of ice samples when coupled with ICP-MS.[24–26] Given its micro-destructive nature and high spatial resolution of sub-millimeter scale, LA serves a dual purpose on ice sampling: (a) minimal sample preparation while the smallest amount of sample possible is used for analysis and (b) ice core analysis achieving a depth resolution of less than 100 μm, producing even two-dimensional impurity images on ice sections.[27] Existing laser ablation systems vary primarily in the type of laser source used and the design of the ablation chamber. The former impacts the methodology for sample removal and the nature of the ablated material for analysis, while the ablation chamber design influences how the sample is collected and delivered to the analyzer, both of which are crucial for accurate analysis.

Laser pulse duration and wavelength stand out as the most investigated parameters that affect the laser-matter interaction, thereby shaping the properties of the removed material.[28–31] Lasers that emit radiation in the infrared (IR) and generate pulses either in the nanosecond[21] or femtosecond regime[32,33] have been utilized for laser ablation on ice samples taking into account the high absorption coefficient of ice at this wavelength.[34] Laser sources emitting at wavelengths of 213 nm (ref. 35 and 36) and 193 nm (ref. 26 and 37) have been shown to couple well enough with ice in spite of its low absorption at these wavelengths.[34] In particular UV excimer lasers at 193 nm achieve controlled ablation with significantly less material removed than with an IR laser source.

Ablation chambers implemented to date come in two designs: open and closed. Open design is used for measurements of entire sections of an ice core cut[35] according to a standard scheme into lengths of either 55 cm or 100 cm for specific analyses. In this configuration, the ablation chamber is positioned above the sample, and it is crucial to establish a secure seal at its base. On the other hand, the closed design is tailored to hold smaller sections of the core within the chamber.[26,38] Advancements in closed system designs include the introduction of a smaller inner cup[39] within the ablation chamber. This modification reduces the dispersion of ablated material both at the site of ablation and along the transfer line, enabling precise adjustment of the carrier gas flow[40] for efficient and reliable delivery to the analyzer.

Exploiting the unique advantages of Laser Ablation as a sampling method, the integration of LA with CRDS is proposed to tackle the intricate challenges involved in water isotope analysis in deep ice cores, offering high-resolution sampling with a more straightforward and accurate depth registration, while at the same time preserving the samples for further analysis. At Ca' Foscari University of Venice, it was the first time, to our knowledge, that water isotope analyses were conducted utilizing a commercial Laser Ablation (LA) system coupled with a Cavity Ring Down Spectrometer (CRDS), with careful adjustments to the coupling protocol already used for LA-ICP-MS[26] and fine-tuning of laser parameters. While the basic working principles of LA sampling remain consistent, significant differences arise when interfacing with a CRDS analyzer, particularly in terms of required water vapour quantities, adopted configurations for collecting and transporting the ablated mass, and the characteristics of the gas ultimately analyzed.

2 Methods

2.1 ns LA – CRDS system

The Laser Ablation – Cavity Ring Down Spectrometer (LA-CRDS) experimental setup for ice is based on the ice core LA-ICP-MS system established at the University of Venice.[26] It comprises three core units: (a) the Laser Ablation (LA) system which incorporates an ArF* excimer laser to generate laser pulses in the nanosecond regime (Analyte Excite+, Teledyne Photon Machines, Bozeman MT, USA), (b) the ablation cryo-

cell (HelEx II 2-volume ablation cell, Teledyne Photon Machines, Bozeman MT, USA) designed for placing the ice sample, where the ablated mass is generated and collected, and (c) the CRDS Water Isotopic Analyzer (L-2130i, PICARRO, Santa Clara CA, USA) employed for conducting water isotope measurements on the ablated samples (Fig. 1). A transport line serves as the conduit connecting the LA system and the CRDS, and delivers the ablated sample from the ablation cell directly to the CRDS cavity for analysis. The microscope system for sample visualization is designed with adjustable magnification and incorporates a high-definition, color GigE camera, positioned perpendicularly to the sample and aligned co-axially with the laser beam. The laser beam and the optical camera move in alignment on the *Z*-axis, facilitating precise focusing of the laser beam onto the sample surface.

2.1.1 Ablation chamber. The two-volume cryo-cell is a closed-chamber configuration which indicates that the ablation chamber accommodates the sample internally (Fig. 1a) as well as an inner cup (Fig. 1b) that surrounds the area where the ablation takes place. The cell is designed with an upper transparent window for observation, while its inner cup features a conically shaped enclosure sealed by an optical window, allowing the laser beam to reach and irradiate the sample. The beam itself is perpendicular relative to the sample plane. The bottom part of the cell houses a specially designed cryogenic sample holder.[26] Through the circulation of a glycol–water mixture cooled at −35 °C, the system ensures the ice sample's surface remains around −23 ± 2 °C.[41] Positioned above the sample surface, the open-bottomed design of the inner cup directs the ablated material into the integrated collection line, using cyclonic flow leading to low-dispersion ablation.[39,42–44] Maintaining a fixed distance between the inner ablation cup and the sample surface ensures a steady sampling environment and a consistent path for gas transfer for every ablation event.

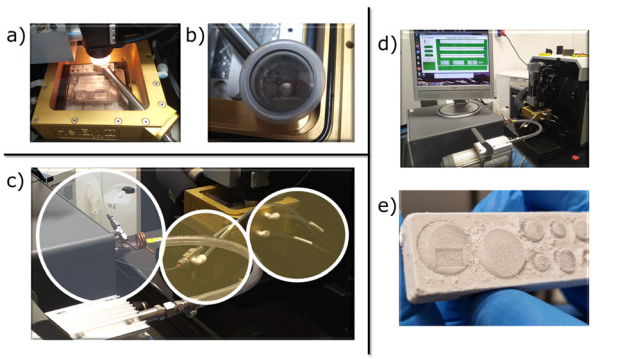

Fig. 1 Detailed view of the LA-CRDS setup and sample processing components. (a) Cryo-cell loaded with samples. (b) Close-up of the ablation chamber's inner cup. (c) Connections for LA – CRDS coupling. (d) The integrated LA-CRDS system. (e) Metal holder containing ice samples. The first cavity shows the result of laser ablation in a raster scan mode, where the material has been removed.

Sample transport is facilitated by the carrier gas which is introduced *via* two independently controlled inlets of the cell: one delivering gas through the HelEx arm to the inner ablation cup, and the second to the main body of the ablation chamber. The outlet of the system, functioning as the collection line, is designed to be co-axial with the carrier gas flow of the arm, and employs a PEEK tube with an outer diameter of 1/16″. This forms a direct link to the CRDS analyzer inlet. The flow rate in both the inner ablation cup and the main body is controlled by software-integrated mass flow controllers, MFC2 and MFC1 respectively, and can be fine-tuned for rapid single pulse respose (SPR) or for maintaining more stable signals, based on the specific requirements of the application. Mounted on a motorized stage, the cryo-cell allows precise micrometric movement for flexible ablation in single-spot, line, or raster scanning modes.

2.1.2 LA-CRDS coupling. Originally designed to interface with an ICP-MS instrument for multi-elemental impurity studies on ice cores,[26,27] the LA system adapted for this study, employing the L-2130i CRDS as the analyzer.[12,45] In the standard operational mode of the L2130-i analyzer, a mixture of water vapour with dry air or nitrogen flows continuously through the cavity. This process stabilizes the cavity at a pressure of 67 mbar and maintains a temperature of 80 °C. The water vapour concentration in the cavity is kept within a range of 1000–30 000 ppm. To ensure a steady flow, the system employs two proportional valves, arranged in a feedback loop, designed to regulate the flow of gas entering (inlet) and exiting (outlet) the cavity, achieving a flow rate of 40 cm^3 min^{-1} in standard condition. For the LA-CRDS operation, nitrogen was selected as the carrier gas, compatible with both the LA chamber and the CRDS cavity. The coupling of the two instruments was established using the PEEK 1/16″ outer diameter transport tubing, extending from the inner ablation cup directly to the CRDS inlet in an open split configuration to stabilize the gas flow to the analyzer. All the connections can be depicted in Fig. 1c and 2.

2.2 Water vapour detection

During LA-CRDS measurements, laser pulses ablate a predefined surface area as the ablation chamber moves in a bidirectional raster scan, continuously transferring ablated ice to the CRDS cavity. Raster scanning mode was selected over line scan and single spot ablation because it produced a continuous stream of freshly ablated material, resulting in a stronger signal in the CRDS analyzer. The produced ablated mass consists of a mixture of aerosol and vapour. The presence of a filter placed directly after the CRDS inlet and before the cavity effectively prevents particles in the aerosol phase from entering the cavity. Each measurement generates a distinct peak for the water vapour signal, as depicted in Fig. 2. This figure further clarifies the measurement process where the laser ablation process is captured in the bidirectional scanning mode: a green spot marks the beginning of laser firing (raster scan) and a red spot denotes the end of the last pulse of the scan. The markers correspond to the green and red dashed lines on

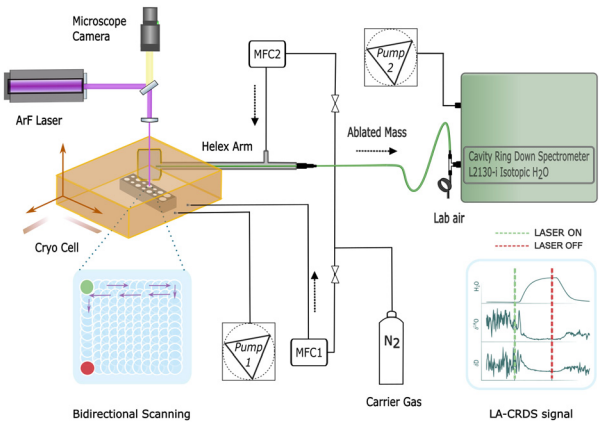

Fig. 2 Schematic diagram of the LA-CRDS experimental setup, highlighting the signal progression captured by the CRDS analyzer during a laser ablation raster scan on an ice sample.

the time series graphs for water vapour, $\delta^{18}O$, and δD. The water vapour signal exhibits a consistent pattern, gradually rising, plateauing during a stable measurement phase, and then returning to the baseline, when no more vapour mass is delivered, as the continuous flow of nitrogen gas removes residual water vapour, before the next measurement preventing interference. This pattern directly corresponds to the $\delta^{18}O$ and δD readings, which also display a phase of stability within the same time intervals during the raster scan.

Optimization of the laser parameters, carrier gas flow rates, and the scanning mode were critical for detecting a relatively high signal for water vapour (H_2O > 2000 ppm) (Fig. S3†) and they are presented in Table 1. The laser settings for the measurements in this study were as follows: the fluence was set between 7 and 10 J cm^{-2}, the repetition rate was 300 Hz, while using a laser spot size of 150 μm. The ablation time was typically set at around 90 seconds covering an area of 4 mm × 4 mm, establishing a 4 mm sampling interval along an ice core's depth (vertical axis of the ice core). The dosage, which defines the number of laser pulses per unit of space, was 12–20 and its high-value results in a better S/N ratio.[46] The flow rates for MFC1 and MFC2 were maintained between 0.1 and 0.15 L min^{-1}. It was observed that lower flow rates and lower pressure (15 PSI to 16 PSI) resulted in a higher and more stable water vapour concentration (Fig. S3†). This suggests a two-phase ablation product: aerosol and vapour. At low pressures, only vapour is transported through the PEEK tube, moving much slower than aerosol under normal conditions, leading to a longer washout period. The resulting water vapour levels detected, between 2000–12 000 ppm, highlight the successful optimization of the LA-CRDS measurement parameters, well above the detection threshold of the CRDS analyzer.

Table 1 LA-CRDS operating parameters

Laser system parameters	
Pulse width	ns
Wavelength	193 nm
Fluence	7 J cm^{-2} to 10 J cm^{-2}
Repetition rate	300 Hz
Spot size	150 μm
Dosage	12–20
Ablation time	≈90 s
Raster scan area	4 mm × 4 mm
Laser ablation cell	
Carrier gas	N_2
MFC1 – ablation chamber	0.1 L min^{-1} to 0.15 L min^{-1}
MFC2 – ablation cup	0.1 L min^{-1} to 0.15 L min^{-1}
Pressure – ablation chamber	15 PSI to 16 PSI
Pressure – ablation cup	15 PSI to 16 PSI
Cavity ring down spectrometer	
Carrier gas	N_2
Cavity pressure	67 mbar
Cavity temperature	80 °C
Flow rate	40 cm^3 min^{-1}
Water vapour	2000 ppm to 12 000 ppm

2.3 Sample preparation

Following the recently established approach for making homogeneous artificial ice standards for calibration of the ICP-MS, we used "method A" described in ref. 47. A metal plate with holes of three distinct sizes (two large at 14.9 mm diameter, six medium at 7.7 mm diameter, and six small at 5.9 mm diameter) served as both the tool for creating the standards and the sample holder for analysis (Fig. 1e). Holes were filled with standard water of known isotopic composition, followed by rapid freezing upon submersion in liquid nitrogen. The resulting ice surface was leveled by scraping with a ceramic ZrO_2 blade (American Cutting Edge, USA), either through manual application or with the blade secured in a custom-designed PTFE vice. This process ensures a uniform distance between the ablation chamber and sample surface for efficient material collection and minimizes signal fluctuations during laser ablation analysis.

3 Results and discussion

3.1 Ice standards characterization

Water isotope measurements were conducted using Discrete Liquid Analysis *via* Cavity Ring-Down Spectroscopy to evaluate the ice standard preparation method. Ice samples were produced from the NS liquid standard (Methods, Section 2.3), extracted from each hole, and melted at room temperature for 10–15 minutes. The resulting liquid samples were analyzed with the CRDS analyzer in Discrete Analysis mode. We collected 400–600 μL of water from large holes, which were individually analyzed. In contrast, meltwater from sets of six medium holes was combined into single samples for analysis. Ice from small holes was not analyzed due to extraction difficulties. The sample preparation procedure was conducted five times, resulting in a total of 15 samples: 10 from the large holes (two per repetition) and 5 from the medium holes (one per repetition, combining meltwater from all six medium holes). Measured isotopic average, after the removal of one

outlier, for $\delta^{18}O$ (−15.17‰, SD = 0.07) and δD (−112.38‰, SD = 0.31) showed no significant deviations from the established true value (−15.37‰ and −112.75‰, respectively). Analysis of isotopic signatures, grouped by hole size, revealed no significant differences, demonstrating water isotopic homogeneity across samples prepared with varying hole sizes. This supports that hole size does not impact measurement accuracy, validating the use of diverse hole sizes for ice sample preparation.

3.2 System performance

3.2.1 System stability. To assess the system's stability, we created an ice standard sample using an adhesive chamber mold attached to a polycarbonate slide, which we filled with the NS water isotope standard following "method C" described in ref. 47. The resulting ice standard sample (65 mm × 22 mm × 0.25 mm) was subjected to laser raster scanning under the optimized experimental conditions outlined in Table 1. The procedure targeted approximately half of the sample's surface for about 7 minutes at a laser fluence of 7 J cm^{-2}. Maintaining a stable signal during continuous laser scanning has been challenging. Fluctuations in the water vapour signal, as shown in Fig. 3a, are most likely attributed to the inherent acceleration and deceleration of the stage during scanning, and the potential irregularities on the sample's surface. Both factors can significantly affect the laser ablation process, leading to variability in both the water vapour signal and isotopic measurements. Allan variance analysis (Fig. 3b), calculated for $\delta^{18}O$ and δD over different integration times using the 6-minute segment of the data (highlighted with grey color (Fig. 3a)), further confirmed this instability. Correcting the isotopic signal for the CRDS analyzer's humidity response did not significantly alter the observed fluctuations (Fig. S1 and S2†). While the fluctuating water vapour levels indicate inconsistencies in the amount of sample ablated and transported to the CRDS analyzer, the uncorrelated isotopic signal suggests additional factors are influencing isotopic measurements, beyond the analyzer's sensitivity to varying water vapour concentrations. These factors might include, but are not limited to, variations in the ablation process itself leading to isotopic fractionation or other complexities related to the overall LA-CRDS analyzer performance. The variability of the isotopic signal over long ablation durations and large sample areas, further supports the chosen approach of discrete sampling, which utilizes short ablation durations (90 seconds) on small sample areas 4 mm × 4 mm and exploits short periods of relative stability to obtain more reliable isotopic data.

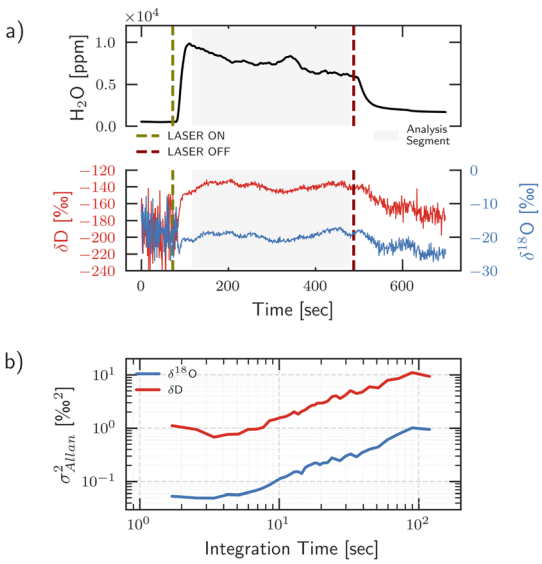

Fig. 3 Water vapour concentration and δD (red) and $\delta^{18}O$ (blue) signal (a) across a 7-minute LA raster scan of NS ice, marked by dashed lines. The grey area highlights the data segment analyzed used for the (b) Allan variance plots for δD and $\delta^{18}O$.

3.2.2 VSMOW two-point calibration. Raw data acquired by the LA-CRDS for $\delta^{18}O$ and δD are derived based on the internal calibration line of the CRDS analyzer. However, to address potential instrumental drift and biases, a VSMOW calibration was performed before proceeding to further data analysis. To implement this, LA-CRDS measurements were conducted on three ice standard samples—TD, NVL, and NS—prepared using the corresponding internal water isotope standards, with known $\delta^{18}O$ and δD values determined *via* conventional CRDS (reported on the VSMOW-SLAP scale in Table 2).

Four samples of each standard were prepared in separate holes in the metal holder. These holes, designated S1, S2, M1, and M2, correspond to different sizes (small hole 1, small hole 2, medium hole 1, and medium size hole 2). All samples representing a single standard were assumed to share a uniform isotopic composition. Three raster scan measurements (4 mm × 4 mm) were conducted per sample: the initial scan at the surface, Layer 1, followed by two measurements, Layer 2 and Layer 3, conducted 100–150 micrometers deeper than the preceding one. This approach aimed to test whether replicate measurements could be obtained from the same area without requiring sample removal or additional preparation steps. The measurement workflow is shown schematically in Fig. 4.

Measurements were conducted on two separate days, utilizing a laser fluence of 8.7 J cm^{-2} on Day 1 and 9.7 J cm^{-2} on Day 2. The data obtained is presented across two graphs (Fig. 5a) for both laser fluence levels, detailed by the sample ID, which integrates the standard name, hole designation, and layer number, reflecting the sequence and depth of measurements. Fig. 5a shows water vapour peaks and the δD signal, with highlighted time windows indicating the LA scanning analysis periods. For constructing a two-point calibration line, the peaks corresponding to Layer 1 of the second replicates measured for the TD and NS standards, specifically 'TD S1 1'

Table 2 Water isotopic composition of liquid laboratory standards

Standard sample	$\delta^{18}O$ [‰]	δD [‰]
TD	−38.82	−307.00
NVL	−31.15	−240.02
NS	−15.37	−112.62

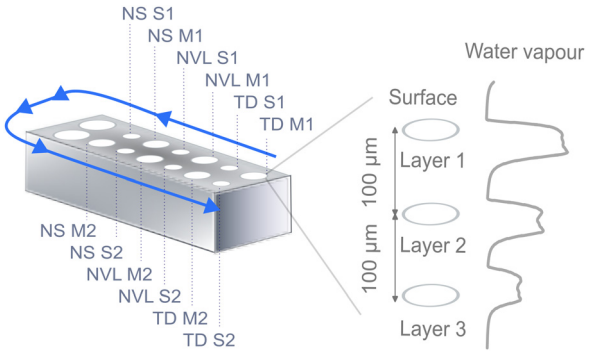

Fig. 4 Schematic of the measurement workflow for three ice standard water LA-CRDS analysis. Four samples per standard (TD, NVL, NS) are placed in specific holder holes (S1, S2, M1, M2). Each sample undergoes three measurements: an initial surface scan (Layer 1) followed by two deeper scans (Layers 2 and 3) at 100 µm intervals. The right panel shows the corresponding water vapour signal for each layer.

and 'NS S1 1' (highlighted in purple), were selected to minimize the impact of potential memory effects from prior measurements. The remaining peaks, depicted in grey, were classified as 'unknowns' to assess the technique's precision and accuracy.

Calibration lines for $\delta^{18}O$ and δD were established based on the mean values of 36 data points collected over a 30-second interval (Fig. 5b), along with their known reference values. The calibration coefficients for $\delta^{18}O$ at a fluence of 8.7 J cm^{-2} are $a_{VSMOW} = 0.99$ and $b_{VSMOW} = 0.32$, and for 9.7 J cm^{-2}, they are $a_{VSMOW} = 0.98$ and $b_{VSMOW} = -1.44$. For δD, the coefficients at 8.7 J cm^{-2} are $a_{VSMOW} = 1.08$ and $b_{VSMOW} = 28.47$, and at 9.7 J cm^{-2}, they are $a_{VSMOW} = 1.09$ and $b_{VSMOW} = 23.99$. The raw time series data were then calibrated using the following formula:

$$\delta_{VSMOW} = a_{VSMOW} \cdot \delta_{measured} + b_{VSMOW} \quad (1)$$

3.2.3 Extraction of VSMOW water isotope values. The water isotopic values were derived by computing the mean and stan-

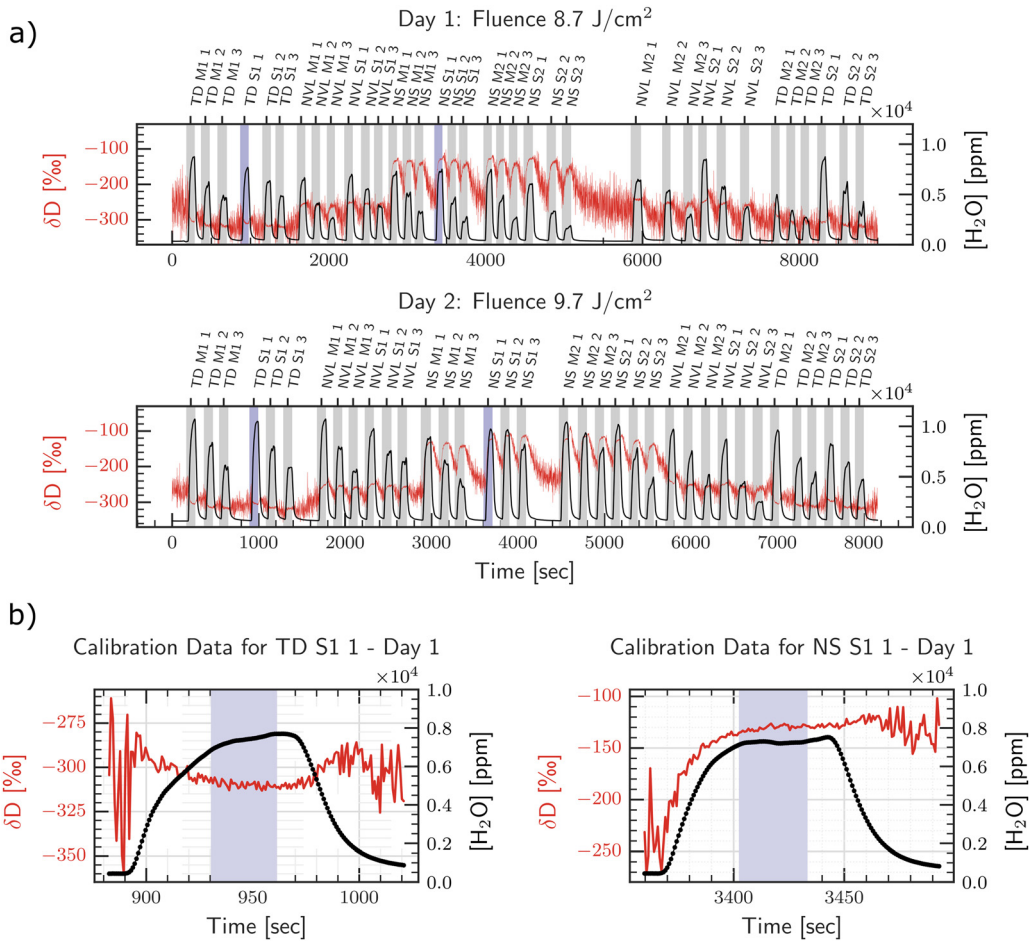

Fig. 5 (a) Time series of δD and water vapour signals for TD, NVL, and NS standards over two days at laser fluences of 8.7 J cm^{-2} (top) and 9.7 J cm^{-2} (bottom). Sample IDs include the standard name, hole designation, and layer number. Shaded regions represent the laser ablation time windows for 'unknown' samples (grey) and calibration peaks (purple). (b) Calibration data showing the selected peaks from the second replicates of TD and NS standards ('TD S1 1' and 'NS S1 1' – Day 1). The shaded regions indicate the 30-second analysis time windows used to determine the mean values for constructing calibration equations.

dard deviation during the stable phase of each peak from the calibrated data, using a 30-second data window. Although minor variations in peak shape were observed due to scanning duration and laser fluence, the data extraction process remained consistent across all peaks with the same time intervals used for statistical analysis. Tables 3 and 4 present the results for all the standard samples measured. The mean standard deviation within individual layers and across all measurements is also detailed, providing insights into measurement repeatability. The corresponding mean deviation from known values is also calculated to offer an assessment of overall accuracy throughout the experimental runs.

The water vapour concentrations, as shown in Tables 3 and 4, vary across layers and fluence levels. At a fluence of 8.7 J cm^{-2}, the highest vapour content is observed in Layer 1 (7205 ppm), decreasing to 3159 ppm in Layer 3. A similar pattern is observed at a higher fluence of 9.7 J cm^{-2} with water vapour content starting at 9335 ppm in Layer 1 and decreasing to 5316 ppm in Layer 3, which suggest that increased laser energy enhances vaporization. This is consistent with previous findings that show that relative amounts of gas and particulate phases produced by laser ablation are dependent on both laser fluence and laser wavelength, with higher energy density and longer wavelengths generating more vapour during laser ablation.[48] However, the decreasing water vapour signals from deeper layers, despite laser focus adjustments by 100–150 μm to compensate for material removal and target subsequent layers, suggest that the initial ablation events may significantly alter the laser-ice interaction leading to less efficient material removal. The ablation process can create an uneven surface through crater formation with microstructural changes which can obscure the camera's view, making it challenging to maintain precise laser focus as ablation progresses. This, in turn, could lead to less efficient laser energy coupling with the target ice layer, resulting in reduced water vapour generation.

Although the calibrated isotopic values for the standards follow the expected trend (Fig. 6a), achieving accurate isotopic measurements for $\delta^{18}O$ and δD remains a significant challenge, for both surface and deeper layers analyzed. The data show increasing mean deviation from known values with

Table 3 Results for ice standards measured at fluence 8.7 J cm^{-2}

ID	$[H_2O]$/ppm	$\delta^{18}O$ (‰)	SD	δD (‰)	SD	$\Delta\delta^{18}O$ (‰)	*Z*-Score	$\Delta\delta D$ (‰)	*Z*-Score
TD M1 1	8480	−38.26	0.36	−300.90	1.77	−0.56	1.55	−6.10	3.46
TD M1 2	5822	−38.92	0.46	−314.05	2.31	0.10	−0.21	7.05	−3.06
TD M1 3	4605	−38.91	0.61	−315.66	2.50	0.09	−0.15	8.66	−3.46
TD S1 1	7374	−38.82	0.30	−307.00	1.99	−0.00	0.00	0.00	0.00
TD S1 2	6242	−39.11	0.39	−315.72	1.88	0.29	−0.74	8.72	−4.64
TD S1 3	4816	−39.08	0.50	−317.79	2.15	0.26	−0.51	10.79	−5.02
NVL M1 1	6403	−31.19	0.37	−248.39	2.48	0.04	−0.11	8.37	−3.37
NVL M1 2	4045	−31.51	0.58	−250.86	2.94	0.36	−0.63	10.84	−3.69
NVL M1 3	2624	−31.34	0.78	−254.24	4.39	0.19	−0.24	14.22	−3.24
NVL S1 1	6737	−31.24	0.31	−243.55	1.75	0.09	−0.28	3.53	−2.02
NVL S1 2	5520	−31.34	0.37	−246.41	2.27	0.19	−0.50	6.39	−2.81
NVL S1 3	3802	−31.38	0.58	−249.12	3.64	0.23	−0.40	9.10	−2.50
NS M1 1	6915	−15.59	0.43	−117.91	2.99	0.23	−0.53	5.29	−1.77
NS M1 2	4888	−15.55	0.54	−117.23	2.62	0.19	−0.36	4.61	−1.76
NS M1 3	3137	−16.56	0.71	−125.36	3.75	1.20	−1.68	12.74	−3.40
NS S1 1	7247	−15.36	0.36	−112.62	2.54	−0.00	0.00	0.00	−0.00
NS S1 2	4347	−15.38	0.61	−116.36	3.30	0.02	−0.03	3.74	−1.13
NS S1 3	2392	−16.46	0.89	−129.47	5.24	1.10	−1.23	16.85	−3.21
NS M2 1	7123	−15.44	0.37	−110.77	1.61	0.08	−0.21	−1.85	1.15
NS M2 2	4418	−15.41	0.43	−114.63	2.91	0.05	−0.12	2.01	−0.69
NS M2 3	2561	−16.26	0.77	−126.83	4.93	0.90	−1.17	14.21	−2.88
NS S2 1	6008	−15.14	0.39	−110.24	2.12	−0.22	0.56	−2.38	1.12
NS S2 2	3248	−15.89	0.61	−120.85	3.38	0.53	−0.87	8.23	−2.44
NS S2 3	1718	−17.05	1.06	−142.16	8.30	1.69	−1.60	29.54	−3.56
NVL M2 1	6385	−30.36	0.36	−234.60	2.71	−0.79	2.17	−5.42	2.00
NVL M2 2	5293	−31.04	0.42	−243.78	2.48	−0.11	0.25	3.76	−1.52
NVL M2 3	2903	−31.12	0.84	−248.16	4.57	−0.03	0.03	8.14	−1.78
NVL S2 1	8398	−31.34	0.39	−240.06	2.14	0.19	−0.48	0.04	−0.02
NVL S2 2	5647	−31.37	0.36	−246.27	2.71	0.22	−0.60	6.25	−2.31
NVL S2 3	3681	−31.56	0.63	−251.62	2.58	0.41	−0.65	11.60	−4.50
TD M2 1	4636	−34.91	0.56	−283.94	3.20	−3.91	6.99	−23.06	7.21
TD M2 2	3196	−37.30	0.57	−305.08	3.83	−1.52	2.70	−1.92	0.50
TD M2 3	2606	−36.89	0.71	−304.19	4.25	−1.93	2.70	−2.81	0.66
TD S2 1	8393	−37.99	0.30	−302.31	1.62	−0.83	2.76	−4.69	2.88
TD S2 2	5241	−38.19	0.50	−311.74	2.49	−0.63	1.27	4.74	−1.90
TD S2 3	3061	−38.09	0.61	−314.91	3.70	−0.73	1.21	7.91	−2.14
Layer 1	**7205**		**0.36**		**2.13**	**−0.20**		**−0.36**	
Layer 2	**4826**		**0.49**		**2.76**	**−0.03**		**5.37**	
Layer 3	**3159**		**0.72**		**4.17**	**0.28**		**11.75**	
All	**4868**		**0.54**		**3.10**	**0.04**		**6.13**	

Table 4 Results for ice standards measured at fluence 9.7 J cm^{-2}

ID	[H_2O]/ppm	$\delta^{18}O$ (‰)	SD	δD (‰)	SD	$\Delta\delta^{18}O$ (‰)	*Z*-Score	$\Delta\delta D$ (‰)	*Z*-Score
TD M1 1	10 214	−39.00	0.36	−306.75	1.33	0.18	−0.49	−0.25	0.19
TD M1 2	8021	−39.16	0.32	−318.39	1.61	0.34	−1.05	11.39	−7.09
TD M1 3	5890	−39.97	0.43	−319.84	1.89	1.15	−2.70	12.84	−6.78
TD S1 1	10 113	−38.83	0.35	−307.05	1.51	0.01	−0.04	0.05	−0.04
TD S1 2	7760	−39.27	0.34	−319.18	1.60	0.45	−1.33	12.18	−7.59
TD S1 3	5888	−39.85	0.42	−321.85	1.78	1.03	−2.44	14.85	−8.32
NVL M1 1	10 297	−32.76	0.38	−252.24	2.69	1.61	−4.28	12.22	−4.54
NVL M1 2	7796	−32.57	0.25	−252.41	2.04	1.42	−5.75	12.39	−6.07
NVL M1 3	5491	−33.49	0.41	−257.33	2.16	2.34	−5.65	17.31	−8.01
NVL S1 1	9313	−33.05	0.40	−247.99	2.09	1.90	−4.70	7.97	−3.80
NVL S1 2	7312	−33.60	0.36	−252.74	2.26	2.45	−6.77	12.72	−5.64
NVL S1 3	6414	−33.46	0.41	−255.37	1.94	2.31	−5.68	15.35	−7.90
NS M1 1	8710	−17.27	0.59	−123.81	3.73	1.91	−3.25	11.19	−3.00
NS M1 2	6313	−16.94	0.34	−122.78	2.50	1.58	−4.64	10.16	−4.06
NS M1 3	4201	−18.70	0.45	−131.96	3.06	3.34	−7.40	19.34	−6.32
NS S1 1	9461	−15.36	0.30	−112.45	2.89	0.00	−0.01	−0.17	0.06
NS S1 2	9538	−13.36	0.35	−100.14	1.90	−2.00	5.74	−12.48	6.57
NS S1 3	7853	−13.11	0.33	−101.35	2.10	−2.25	6.89	−11.27	5.38
NS M2 1	10 220	−15.49	0.24	−111.07	2.33	0.13	−0.55	−1.55	0.67
NS M2 2	9105	−13.92	0.49	−103.68	3.00	−1.44	2.95	−8.94	2.98
NS M2 3	7447	−14.09	0.32	−106.34	2.64	−1.27	3.99	−6.28	2.38
NS S2 1	9838	−16.91	0.29	−114.14	2.33	1.55	−5.31	1.52	−0.65
NS S2 2	6944	−16.44	0.34	−118.03	2.44	1.08	−3.22	5.41	−2.21
NS S2 3	4216	−18.24	0.63	−130.05	3.67	2.88	−4.56	17.43	−4.75
NVL M2 1	9193	−32.48	0.41	−239.65	1.88	1.33	−3.29	−0.37	0.20
NVL M2 2	6868	−32.46	0.36	−248.75	2.12	1.31	−3.65	8.73	−4.11
NVL M2 3	4683	−33.25	0.47	−254.56	2.12	2.10	−4.46	14.54	−6.84
NVL S2 1	8142	−32.42	0.54	−247.09	1.99	1.27	−2.37	7.07	−3.55
NVL S2 2	4254	−33.57	0.58	−255.30	3.08	2.42	−4.18	15.28	−4.97
NVL S2 3	2485	−34.21	0.74	−259.01	5.83	3.06	−4.14	18.99	−3.26
TD M2 1	9308	−38.81	0.30	−305.07	1.81	−0.01	0.03	−1.93	1.07
TD M2 2	6472	−38.83	0.38	−312.07	2.45	0.01	−0.03	5.07	−2.07
TD M2 3	4744	−39.23	0.47	−315.75	3.17	0.41	−0.86	8.75	−2.76
TD S2 1	8112	−38.01	0.38	−298.90	1.78	−0.81	2.13	−8.10	4.54
TD S2 2	6144	−39.66	0.38	−318.80	2.05	0.84	−2.21	11.80	−5.76
TD S2 3	4478	−40.20	0.52	−321.79	2.72	1.38	−2.68	14.79	−5.45
Layer 1	**9335**		**0.39**		**2.20**	**0.91**		**2.78**	
Layer 2	**7211**		**0.37**		**2.25**	**0.70**		**6.97**	
Layer 3	**5316**		**0.47**		**2.76**	**1.37**		**11.38**	
All	**7167**		**0.41**		**2.41**	**1.00**		**7.30**	

sample depth, indicating reduced accuracy for subsequent layers analyzed at greater depths. At a fluence of 8.7 J cm^{-2}, mean deviation for $\delta^{18}O$ is −0.20‰ in Layer 1, −0.03‰ in Layer 2, and 0.28‰ in Layer 3, while for δD, it is −0.36‰, 5.37‰, and 11.75‰, respectively. This trend is exacerbated at a higher fluence of 9.7 J cm^{-2} especially for $\delta^{18}O$, with the deviation increasing at 0.91‰ in Layer 1, 0.70‰ in Layer 2, and 1.37‰ in Layer 3, indicating a pronounced influence of fluence on measurement accuracy. At the same laser fluence, deviation values for δD are 2.78‰, 6.97‰, and 11.38‰, for the respective layers.

The deviation from the known values (Fig. 6b) shows a slight trend towards isotopic depletion for both $\delta^{18}O$ and δD, although it exhibits some variability, indicating both depletion and enrichment. This trend is particularly pronounced at higher laser fluences, suggesting that isotopic fractionation towards lighter isotopes in the analyzed vapour phase is amplified with increasing laser energy input. The data further prove that, on average, the measured isotopic values tend to be lower than the expected values. Both elemental and isotopic fractionation have been investigated in aerosols produced by LA and analyzed by ICP-MS, with studies indicating that more volatile species are present in the gas phase rather than in the particulate phase,[49–52] which in this study would partially explain the depleted gas phase. Other effects like melting zones and recondensation which are linked with the ablation process could also contribute to the overall fractionation. However, understanding the mechanisms underlying isotopic fractionation of the gas-phase product during LA-CRDS is beyond the scope of this study.

In depth profile analysis, it was observed that the most substantial fractionation occurs in deeper layers, particularly when considering δD values. The higher fluence causes greater deviations but follows a similar trend for the accuracy over multiple layers. Both the efficiency of material removal and the accuracy of isotopic measurements are influenced by the accumulating effects of prior ablations which alter the microenvironment, including structural modifications and recondensation, and so the exposed surface for each subsequent analysis. Therefore, observed deviations from expected values

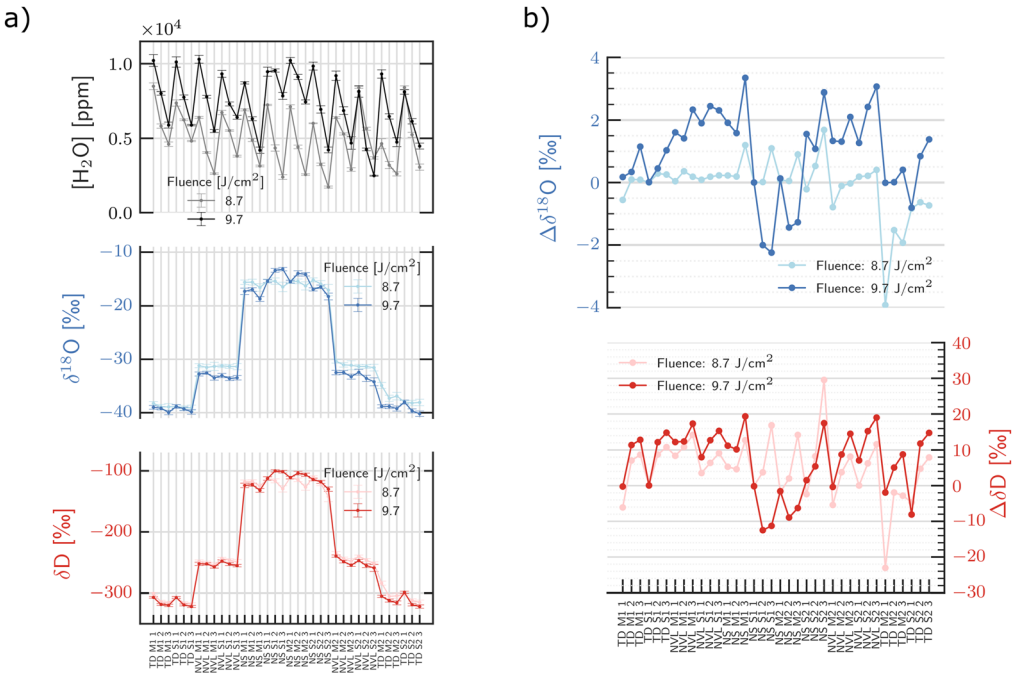

Fig. 6 Calibrated results for TD, NVL, NS ice standard samples (a) and difference between known and calibrated values of $\delta^{18}O$ and δD (b), analyzed at fluences of 8.7 and 9.7 J cm^{-2}.

in deeper layers, along with reduced water vapour signals, highlight the complex relationship between laser fluence, ice matrix properties, and effects of previous ablation events.

The mean SD values that were calculated for each layer, reveal a clear trend in the measurement variability: as water vapour content increases, the standard deviation for both isotopes decrease, suggesting higher water vapour content leads to more precise isotopic measurements. Specifically, at a fluence of 8.7 J cm^{-2}, the average standard deviation for $\delta^{18}O$ ranges from 0.36‰ in Layer 1 to 0.72‰ in Layer 3, with deeper layers represented by lower water vapour levels, and for δD from 2.13‰ to 4.17‰, while at 9.7 J cm^{-2}, the average standard deviation values for $\delta^{18}O$ range from 0.39‰ to 0.47‰ and δD from 2.20‰ to 2.76‰ for the respective layers.

Fig. 7 shows the relationship between the standard deviation of $\delta^{18}O$ and δD with water vapour content at both fluence levels. The increase in the mass of ice ablated, which is reflected in the higher production of water vapour contributes to more stable isotopic measurements. Standard deviation values for both $\delta^{18}O$ and δD decrease up to a water vapour concentration until they reach a plateau between 6000–8000 ppm achieved at a fluence of 8.7 J cm^{-2}. This trend of decreasing variability with increasing water vapour concentration is similarly observed at higher energy of 9.7 J cm^{-2}; however, the initial standard deviations are lower due to the greater mass ablated, leading to a high signal captured in the detector.

Despite these observations, when the humidity concentration exceeds 8000 ppm, specifically at 9.7 J cm^{-2}, there is an observed increase in the variability of standard deviation

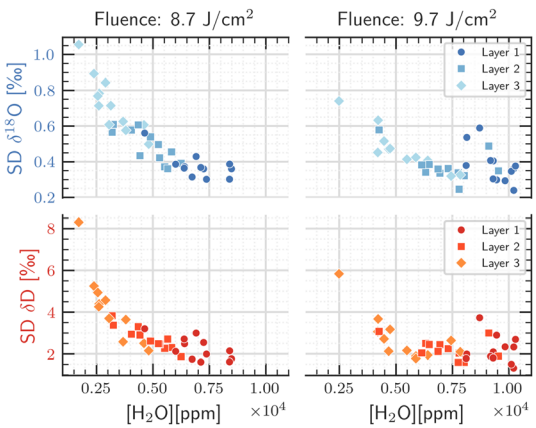

Fig. 7 Standard deviation of isotopic ratios $\delta^{18}O$ and δD across different fluence levels and layers plotted against the mean water vapour concentration for ice standards data.

values. This increase, despite the generation of more water vapour, likely results from further enhanced but "uncontrolled" ablation. Uncontrolled ablation seems to produce variable amounts of ablated mass and consequently variable water vapour levels, as evidenced by the mean water vapour values for each layer (in ppm), along with the average of their respective standard deviations (8.7 J cm^{-2}: 7205 (Mean SD: 100), 4826 (Mean SD: 117), 3159 (Mean SD: 99) and 9.7 J cm^{-2}: 9335 (Mean SD: 255), 7211 (Mean SD: 155), 5316 (Mean SD: 184)). Increased fluctuations in uncontrolled water vapour production may introduce variability in isotopic fractionation,

ultimately compromising the precision of isotopic measurements. A similar transition between a well-defined and an enhanced but uncontrolled ablation regime has been previously described in the study of impurities in ice cores through LA-ICP-MS. Although observed at a lower fluence threshold than in this study, an additional dependency was found for ice impurity standards on their elemental concentration, laser spot size and fluence.[47] The results obtained here further highlight this crucial consideration for LA-CRDS analysis of ice: the need to balance sufficient water vapour generation for robust signal intensity with maintaining a controlled ablation process to minimize isotopic fractionation arising from variable ablation volumes, especially at higher fluences.

3.3 LA-CRDS on Antarctic ice core section

A 50 mm × 10 mm section of an ice core from Neumayer Station, Antarctica, was measured by LA-CRDS. The cutting scheme of the core is shown in Fig. S4.† Measurements were conducted on 4 mm × 4 mm segments, covering the ice section (Fig. S5†) as depicted in the schematic of the laser scanning pattern (Fig. 8). Surface measurements with a laser fluence of 8.7 J cm^{-2} (TEDRIST 1 and TEDRIST 2, indicated in blue) were performed on the same day the standards were measured with the same fluence (Day 1). Subsequent measurements targeted a deeper part of the core at a higher laser fluence of 9.7 J cm^{-2} (TEDRIST 3, in dark blue), conducted on the same day as the standards measured with 9.7 J cm^{-2} (Day 2). For these latter measurements, the previously ablated area was scraped to ensure a clean flat surface for analysis. Ice core data were calibrated using the specific calibration lines developed for each fluence level, with final isotopic values calculated by averaging data over consistent 30-second intervals. The results for all variables measured, including water vapour, δ^{18}O, and δD, are presented in Tables 5 and 6.

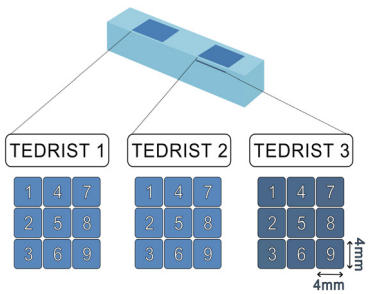

Fig. 8 Schematic diagram of the laser scanning pattern on the TEDRIST ice core section. The areas are divided into three TEDRIST regions with different fluence levels used during LA-CRDS analysis. TEDRIST 1 and TEDRIST 2 were ablated with a laser fluence of 8.7 J cm^{-2} and TEDRIST 3 with 9.7 J cm^{-2}.

The water vapour concentrations produced in both laser fluence levels are similar, unlike the vapour produced when ice standards were analyzed, where higher fluence resulted in higher water vapour concentrations. This suggests that the laser couples differently with the ice core compared to the ice standards. Additionally, the water vapour levels for the ice core are lower than those obtained for the respective fluence during surface measurements on the ice standards, further indicating a distinct interaction between the laser and different ice matrices.

The calibrated isotopic values were compared against the reference water isotope values determined by Discrete-CRDS Analysis (δ^{18}O: −21.34‰ and δD: −165.4‰). The isotopic measurements of δ^{18}O and δD for the ice core data reveal significant deviations from expected values (Fig. 9). At the lower laser fluence of 8.7 J cm^{-2}, both δ^{18}O and δD values are overestimated, as indicated by the mean deviations (δ^{18}O = −1.47‰ and δD = −4.77‰) and *Z*-scores in Table 5. On the other hand, at the higher fluence of 9.7 J cm^{-2}, an underestimation is evident, with mean deviations (δ^{18}O = 1.28‰ and δD = 8.94‰) as shown in Table 6. The deviation of the derived iso-

Table 5 Results for TEDRIST ice core section measured at fluence 8.7 J cm^{-2}

ID	[H_2O]/ppm	δ^{18}O (‰)	SD	δD (‰)	SD	$\Delta\delta^{18}$O (‰)	*Z*-Score	$\Delta\delta$D (‰)	*Z*-Score
TEDRIST 1	5599	−20.00	0.37	−162.92	2.55	−1.34	3.62	−2.48	0.97
TEDRIST 2	4980	−20.10	0.41	−162.96	2.24	−1.24	3.00	−2.44	1.09
TEDRIST 3	4783	−20.39	0.49	−162.90	2.57	−0.95	1.94	−2.50	0.97
TEDRIST 4	4387	−19.99	0.40	−160.02	2.42	−1.35	3.36	−5.38	2.22
TEDRIST 5	6033	−19.59	0.50	−157.87	2.12	−1.75	3.50	−7.53	3.55
TEDRIST 6	5943	−19.97	0.38	−161.20	2.09	−1.37	3.60	−4.20	2.02
TEDRIST 7	6078	−19.58	0.33	−157.80	1.99	−1.76	5.32	−7.60	3.82
TEDRIST 8	5853	−19.41	0.37	−157.49	1.83	−1.93	5.16	−7.91	4.32
TEDRIST 9	6149	−20.05	0.40	−160.23	2.00	−1.29	3.24	−5.17	2.58
TEDRIST 10	5188	−20.65	0.43	−165.88	3.42	−0.69	1.62	0.48	−0.14
TEDRIST 11	4844	−20.09	0.51	−160.62	2.88	−1.25	2.45	−4.78	1.66
TEDRIST 12	4197	−19.72	0.60	−159.30	5.26	−1.62	2.72	−6.10	1.16
TEDRIST 13	5473	−19.53	0.47	−159.85	2.61	−1.81	3.83	−5.55	2.13
TEDRIST 14	5088	−19.45	0.40	−158.07	3.72	−1.89	4.70	−7.33	1.97
TEDRIST 15	4853	−19.50	0.45	−158.69	2.59	−1.84	4.05	−6.71	2.59
TEDRIST 16	5230	−19.85	0.49	−164.48	3.69	−1.49	3.04	−0.92	0.25
TEDRIST 17	4830	−19.55	0.46	−160.39	3.38	−1.79	3.89	−5.01	1.48
TEDRIST 18	5187	−20.23	0.46	−160.62	2.45	−1.11	2.44	−4.78	1.95
All	**5261**		**0.44**		**2.77**	**−1.47**		**−4.77**	

Table 6 Results for TEDRIST ice core section measured at fluence 9.7 J cm^{-2}

ID	[H_2O]/ppm	$\delta^{18}O$ (‰)	SD	δD (‰)	SD	$\Delta\delta^{18}O$ (‰)	*Z*-Score	$\Delta\delta D$ (‰)	*Z*-Score
TEDRIST 1	5176	−23.18	0.41	−172.04	3.00	1.84	−4.49	6.64	−2.22
TEDRIST 2	5594	−23.01	0.44	−174.87	2.88	1.67	−3.79	9.47	−3.29
TEDRIST 3	4597	−23.33	0.55	−177.35	3.31	1.99	−3.61	11.95	−3.61
TEDRIST 4	4831	−23.07	0.36	−177.40	3.15	1.73	−4.77	12.00	−3.81
TEDRIST 5	5577	−22.32	0.44	−173.33	2.81	0.98	−2.22	7.93	−2.82
TEDRIST 6	6200	−21.47	0.40	−169.25	2.61	0.13	−0.33	3.85	−1.47
TEDRIST 7	5303	−22.22	0.45	−174.04	2.69	0.88	−1.93	8.64	−3.21
TEDRIST 8	4426	−22.96	0.47	−176.60	2.88	1.62	−3.44	11.20	−3.89
TEDRIST 9	5262	−21.98	0.43	−174.23	2.88	0.64	−1.48	8.83	−3.06
All	**5218**		**0.44**		**2.91**	**1.28**		**8.94**	

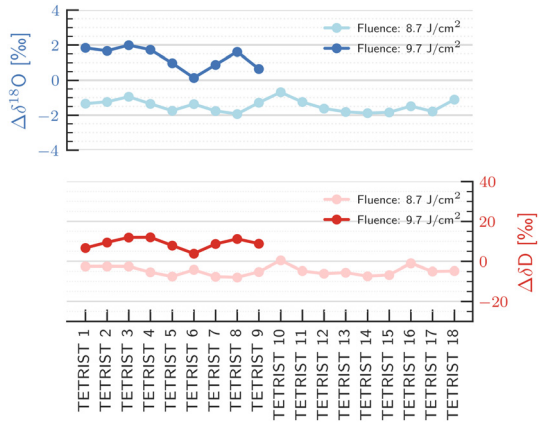

Fig. 9 Difference between known and calibrated values of $\delta^{18}O$ and δD for the ice core section at laser fluences of 8.7 and 9.7 J cm^{-2}.

topic values from expected values on ice core analysis do not align well with those obtained on ice standards, despite using the same calibration parameters for each fluence, likely because the calibration standards are not fully matrix matched, as some differences in ablation characteristics have been observed between artifical and glacier ice at high fluences.[47]

The mean standard deviation values for $\delta^{18}O$ and δD indicate that the variability for the two sets of measurements is similar, likely due to the similar water vapour levels, and closely matches the values obtained for the ice standards at the same water vapour concentration range. Although the isotopic fractionation response to laser fluence is non-uniform, the similar measurement variability suggests that the method maintains a level of consistency comparable to that of the ice standards.

3.4 LA-CRDS in ice core isotope analysis

Unlike the existing ice sampling methods in ice core studies, which are combined with a CRDS analyzer, and require either the discrete melting of cut ice pieces (10 mm in length) or the continuous melting/vaporizing of an entire ice core section (55 cm or 100 cm in length) for water isotope analysis,[16] the laser ablation system presented here showed capabilities of minimal sample preparation and sample consumption that allow the preservation of the analyzed sample for further analysis. Laser ablation offers the possibility for accurate depth registration which is critical for the extraction of high-quality isotopic time series. The new system can analyze samples with maximum dimensions of 50 mm × 10 mm × 10 mm, achieving a sampling resolution of 4 mm, comparable to that achieved by conventional sampling methods, with potential for even higher resolution, crucial for both resolving thin layers in the deep sections of an ice core and restoring isotopic signal, achieving high-resolution temporal profiles. Sequential ablation scans over the same area are not recommended. The challenges associated with refocusing the laser beam due to crater formation and the potential alteration of isotopic composition in deeper layers by recondensation processes can compromise the accuracy of the measurements. Despite current limitations in precision and accuracy, the qualitative agreement between observed and established values opens new possibilities for ice core research highlighting the method's promise for future applications in water isotope analysis. Implementing the LA-CRDS technique in ice core studies necessitates the use of a laser source with properties that minimize laser ablation-induced isotopic fractionation while generating high concentrations of water vapour. Testing high power lasers with shorter pulse durations could potentially meet these requirements and achieve the highest possible resolution, ideally extending to the micrometer scale. Additionally, developing larger ablation chambers to accommodate standard ice core dimensions will broaden the applicability of this technique. These advancements will enable LA-CRDS to function as a micro-destructive method, providing high-quality water isotope data with the precision and accuracy needed to capture even the most intricate climate signals, potentially in a continuous mode.

4 Conclusions

This study presents a novel technique for analyzing water isotopes in ice samples by coupling a commercial laser ablation system, equipped with a nanosecond ArF (193 nm) laser, with a CRDS water isotope analyzer. This method successfully generates a gas phase product from ablated ice for isotopic analysis. A discrete sampling approach ensures relatively stable

water vapour and corresponding water isotope signals, enabling qualitative isotopic characterization. Water vapour production and isotopic composition, calibrated to the VSMOW-SLAP scale, exhibit strong dependence on laser ablation parameters. Sequential ablation at greater depths of ice standards revealed reduced water vapour levels and increasing isotopic deviations with successive ablations, likely due to a complex interplay between challenging refocusing conditions with depth and fractionation due to recondensation of the pre-ablated material. Surface measurements also displayed discrepancies, potentially arising from ablation-induced fractionation or transport effects, with higher fluences exacerbating these deviations. Ice core analysis further confirmed that the observed signal variability originated from limitations in the laser ablation system's performance, rather than inhomogeneities within the ice standards and introduced the need for matrix-matched standards that demonstrate a comparable ablation response to ice core samples. Unlocking the full potential of high-resolution LA-CRDS for ice core analysis requires lasers with high power output and short pulse durations to enhance water vapour generation from sample areas smaller than the millimeter scale, while minimizing laser-induced isotopic fractionation, ultimately enabling the extraction of detailed high-quality paleoclimatic records.

Data availability

Data for this article, including liquid CRDS analysis on ice standards and LA-CRDS on ice standards and ice core samples are available at Zenodo: LA_CRDS_WATER_ISOTOPE_ICE_CORES_RAW_DATA at **https://doi.org/10.5281/zenodo.13152033**.

The code used for data analysis is available on GitHub at: **https://github.com/EiriniNBI/LA_CRDS_Water_Isotope.git**.

Conflicts of interest

The authors have declared that there are no potential conflicts of interest.

Acknowledgements

The authors would like to thank Maria Hörhold, Melanie Behrens and Matthias Hüther from Alfred Wegener Institute for providing the TEDRIST sample used for intercomparison exercises within the BEOIC (Beyond Epica-Oldest Ice Core) Water Isotope Consortium, which was instrumental in this study for testing the LA-CRDS technique. This work has received funding by the European Union's Horizon 2020 Research and Innovation Program under Marie Sklodowska-Curie Grant Agreement No. 955750. Pascal Bohleber gratefully acknowledges funding from the European Union's Horizon 2020 Research and Innovation Program under the Marie Skłodowska-Curie Grant Agreement No. 101018266. Vasileios Gkinis acknowledges support from the Villum Foundation (Project No. 00022995, 00028061), the Danish Independent Research Fund (DFF Grant No. 10.46540/2032-00228B) and Carlsberg Foundation (project 2013_01_0899, CF21-0199).

References

1 J. Jouzel and V. Masson-Delmotte, *Quat. Sci. Rev.*, 2010, **29**, 3683–3689.
2 J. Jouzel, *Water Stable Isotopes: Atmospheric Composition and Applications in Polar Ice Core Studies*, Elsevier, 2014, pp. 213–256.
3 *Environmental Isotopes in The Hydrological Cycle*, ed. W. Mook, International Atomic Energy Agency and United Nations Educational, Scientific and Cultural Organization, 2000, vol. 1.
4 W. Dansgaard, *Tellus A*, 2012, **16**, 436.
5 E. C. Members, *Nature*, 2004, **429**, 623–628.
6 N. Members, *Nature*, 2004, **431**, 147–151.
7 D. A. Lilien, D. Steinhage, D. Taylor, F. Parrenin, C. Ritz, R. Mulvaney, C. Martín, J.-B. Yan, C. O'Neill, M. Frezzotti, H. Miller, P. Gogineni, D. Dahl-Jensen and O. Eisen, *Cryosphere*, 2021, **15**, 1881–1888.
8 A. Chung, F. Parrenin, D. Steinhage, R. Mulvaney, C. Martín, M. G. P. Cavitte, D. A. Lilien, V. Helm, D. Taylor, P. Gogineni, C. Ritz, M. Frezzotti, C. O'Neill, H. Miller, D. Dahl-Jensen and O. Eisen, *Cryosphere*, 2023, **17**, 3461–3483.
9 C. Holme, V. Gkinis and B. M. Vinther, *Geochim. Cosmochim. Acta*, 2018, **225**, 128–145.
10 K. Pol, V. Masson-Delmotte, S. Johnsen, M. Bigler, O. Cattani, G. Durand, S. Falourd, J. Jouzel, B. Minster, F. Parrenin, C. Ritz, H. Steen-Larsen and B. Stenni, *Earth Planet. Sci. Lett.*, 2010, **298**, 95–103.
11 F. S. L. Ng, *Cryosphere*, 2023, **17**, 3063–3082.
12 E. Crosson, *Appl. Phys. B: Lasers Opt.*, 2008, **92**, 403–408.
13 E. Kerstel and L. Gianfrani, *Appl. Phys. B: Lasers Opt.*, 2008, **92**, 439–449.
14 I. S. Begley and C. M. Scrimgeour, *Anal. Chem.*, 1997, **69**, 1530–1535.
15 M. Gehre, H. Geilmann, J. Richter, R. A. Werner and W. A. Brand, *Rapid Commun. Mass Spectrom.*, 2004, **18**, 2650–2660.
16 V. Gkinis, T. J. Popp, T. Blunier, M. Bigler, S. Schüpbach, E. Kettner and S. J. Johnsen, *Atmos. Meas. Tech.*, 2011, **4**, 2531–2542.
17 B. D. Emanuelsson, W. T. Baisden, N. A. N. Bertler, E. D. Keller and V. Gkinis, *Atmos. Meas. Tech.*, 2015, **8**, 2869–2883.
18 T. R. Jones, J. W. C. White, E. J. Steig, B. H. Vaughn, V. Morris, V. Gkinis, B. R. Markle and S. W. Schoenemann, *Atmos. Meas. Tech.*, 2017, **10**, 617–632.
19 E. J. Steig, T. R. Jones, A. J. Schauer, E. C. Kahle, V. A. Morris, B. H. Vaughn, L. Davidge and J. W. White, *Front. Earth Sci.*, 2021, **9**, 640292.

20 R. E. Russo, X. Mao and O. V. Borisov, *TrAC, Trends Anal. Chem.*, 1998, **17**, 461–469.
21 H. Reinhardt, M. Kriews, H. Miller, O. Schrems, C. Lüdke, E. Hoffmann and J. Skole, *Anal. Bioanal. Chem.*, 2001, **370**, 629–636.
22 M. Burger, P. J. Skrodzki, L. A. Finney, J. Hermann, J. Nees and I. Jovanovic, *Phys. Plasmas*, 2018, **25**(8), 083115.
23 C. Li, Q. Li, L. Li, B. Men, H. Wu, D. Wu, R. Hai, X. Wu and H. Ding, *Spectrochim. Acta, Part B*, 2023, **206**, 106735.
24 H. Reinhardt, M. Kriews, H. Miller, C. Lüdke, E. Hoffmann and J. Skole, *Anal. Bioanal. Chem.*, 2003, **375**, 1265–1275.
25 W. Müller, J. M. G. Shelley and S. O. Rasmussen, *J. Anal. At. Spectrom.*, 2011, **26**, 2391.
26 P. Bohleber, M. Roman, M. Šala and C. Barbante, *J. Anal. At. Spectrom.*, 2020, **35**, 2204–2212.
27 P. Bohleber, M. Roman, M. Šala, B. Delmonte, B. Stenni and C. Barbante, *Cryosphere*, 2021, **15**, 3523–3538.
28 B. N. Chichkov, C. Momma, S. Nolte, F. Alvensleben and A. Tünnermann, *Appl. Phys. A: Mater. Sci. Process.*, 1996, **63**, 109–115.
29 F. Poitrasson, X. Mao, S. S. Mao, R. Freydier and R. E. Russo, *Anal. Chem.*, 2003, **75**, 6184–6190.
30 J. Koch, S. Schlamp, T. Rösgen, D. Fliegel and D. Günther, *Spectrochim. Acta, Part B*, 2007, **62**, 20–29.
31 M. Shaheen, J. Gagnon and B. Fryer, *Chem. Geol.*, 2012, **330–331**, 260–273.
32 K. M. Peensoo, MSc thesis, *Physics of Ice, Climate and Earth*, University of Copenhagen, 2021.
33 E. Malegiannaki, K. M. Peensoo, P. Bohleber and V. Gkinis, *Past Global Changes Magazine*, 2023, vol. 31, pp. 64–65.
34 S. G. Warren and R. E. Brandt, *J. Geophys. Res.: Atmos.*, 2008, **113**, D14220.
35 S. B. Sneed, P. A. Mayewski, W. Sayre, M. J. Handley, A. V. Kurbatov, K. C. Taylor, P. Bohleber, D. Wagenbach, T. Erhardt and N. E. Spaulding, *J. Glaciol.*, 2015, **61**, 233–242.
36 N. E. Spaulding, S. B. Sneed, M. J. Handley, P. Bohleber, A. V. Kurbatov, N. J. Pearce, T. Erhardt and P. A. Mayewski, *Environ. Sci. Technol.*, 2017, **51**, 13282–13287.
37 D. Della Lunga, W. Müller, S. O. Rasmussen and A. Svensson, *J. Glaciol.*, 2014, **60**, 970–988.
38 D. Della Lunga, W. Müller, S. O. Rasmussen, A. Svensson and P. Vallelonga, *Cryosphere*, 2017, **11**, 1297–1309.
39 S. J. M. Van Malderen, A. J. Managh, B. L. Sharp and F. Vanhaecke, *J. Anal. At. Spectrom.*, 2016, **31**, 423–439.
40 T. V. Acker, S. J. V. Malderen, T. Buckle and F. Vanhaecke, *High-speed sub-micrometer imaging of sub-cellular structures in single cells using ARIS*, Teledyne Cetac Technologies Inc. technical report, 2017.
41 P. Bohleber, N. Stoll, M. Rittner, M. Roman, I. Weikusat and C. Barbante, *Geochem., Geophys., Geosyst.*, 2023, **24**, e2022GC010595.
42 S. M. Eggins, R. Grün, M. T. McCulloch, A. W. Pike, J. Chappell, L. Kinsley, G. Mortimer, M. Shelley, C. V. Murray-Wallace, C. Spötl and L. Taylor, *Quat. Sci. Rev.*, 2005, **24**, 2523–2538.
43 D. N. Douglas, A. J. Managh, H. J. Reid and B. L. Sharp, *Anal. Chem.*, 2015, **87**, 11285–11294.
44 S. J. Van Malderen, T. Van Acker and F. Vanhaecke, *Anal. Chem.*, 2020, **92**, 5756–5764.
45 E. J. Steig, V. Gkinis, A. J. Schauer, S. W. Schoenemann, K. Samek, J. Hoffnagle, K. J. Dennis and S. M. Tan, *Atmos. Meas. Tech.*, 2014, **7**, 2421–2435.
46 M. Šala, V. S. Šelih, C. C. Stremtan, T. Tămaş and J. T. van Elteren, *J. Anal. At. Spectrom.*, 2021, **36**, 75–79.
47 P. Bohleber, P. Larkman, N. Stoll, D. Clases, R. Gonzalez de Vega, M. Šala, M. Roman and C. Barbante, *Geochem., Geophys., Geosyst.*, 2024, **25**, e2023GC011425.
48 T. Van Helden, K. Mervič, I. Nemet, J. T. van Elteren, F. Vanhaecke, S. Rončević, M. Šala and T. Van Acker, *Anal. Chim. Acta*, 2024, **1287**, 342089.
49 J.-L. Todol and J.-M. Mermet, *Spectrochim. Acta, Part B*, 1998, **53**, 1645–1656.
50 H.-R. Kuhn and D. Günther, *Anal. Chem.*, 2003, **75**, 747–753.
51 S. E. Jackson and D. Günther, *J. Anal. At. Spectrom.*, 2003, **18**, 205–212.
52 H.-R. Kuhn, N. J. Pearson and S. E. Jackson, *J. Anal. At. Spectrom.*, 2007, **22**, 547.